# DVB-S Based Passive Polarimetric ISAR—Methods and Experimental Validation

Iole Pisciottano, *Graduate Student Member, IEEE*, Fabrizio Santi, *Member, IEEE*, Debora Pastina, *Member, IEEE*, and Diego Cristallini

Abstract—**In this work, we focus on passive polarimetric ISAR for ship target imaging using DVB-S signals of opportunity. A first goal of the research is to investigate if, within the challenging passive environment, different scattering mechanisms, belonging to distinct parts of the imaged target, can be separated in the polarimetric domain. Furthermore, a second goal is at verifying if polarimetric diversity could enable the formation of ISAR products with enhanced quality with respect to the single channel case, particularly in terms of better reconstruction of the target shape. To this purpose, a dedicated trial has been conducted along the river Rhine in Germany by means of an experimental DVB-S based system developed at Fraunhofer FHR and considering a ferry as cooperative target. To avoid inaccuracies due to data-driven motion compensation procedures and to fairly interpret the polarimetric results, we processed the data by means of a known-motion back-projection algorithm obtaining ISAR images at each polarimetric channel. Then, different approaches in the polarimetric domain have been introduced. The first one is based on the well-known Pauli Decomposition. The others can be divided in two main groups: (i) techniques aimed at separating the different backscattering mechanisms, and (ii) image domain techniques to fuse the polarimetric information in a single ISAR image with enhanced quality. The different considered techniques have been applied to several data sets with distinct bistatic geometries. The obtained results clearly demonstrate the potentialities of polarimetric diversity that could be fruitfully exploited for classification purposes.**

Index Terms—**Passive ISAR, polarimetric data, satellite signals of opportunity, DVB-S-based passive radar.**
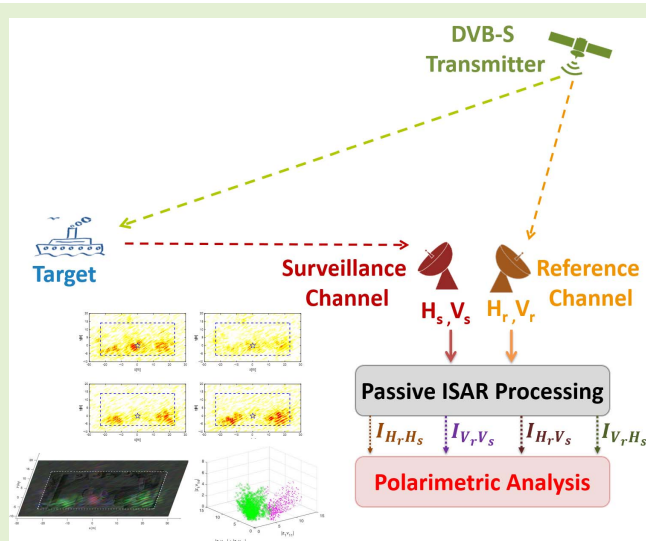
I. INTRODUCTION

NOWADAYS passive radar sensors are the object of a rising interest by the worldwide scientific community. The exploitation of existing transmissions offers an exciting chance to perform radar tasks with no requirements for a dedicated transmitting segment. This lowers the costs of the

Iole Pisciottano is with the PSR Department, Fraunhofer Institute for High Frequency Physics and Radar Techniques FHR, 53343 Wachtberg, Germany, and also with the DIET Department, University of Rome "La Sapienza," 00184 Rome, Italy (e-mail: iole.pisciottano@fhr.fraunhofer.de).

Fabrizio Santi and Debora Pastina are with the DIET Department, University of Rome "La Sapienza," 00184 Rome, Italy (e-mail: fabrizio.santi@uniroma1.it; debora.pastina@uniroma1.it).

Diego Cristallini is with the PSR Department, Fraunhofer Institute for High Frequency Physics and Radar Techniques FHR, 53343 Wachtberg, Germany (e-mail: diego.cristalllini@fhr.fraunhofer.de).

Digital Object Identifier 10.1109/JSEN.2020.3037091

system and its maintenance and enables covert operations, nicely without additional spectral requirements. Moreover, the system is totally 'green', as it does not emit e.m. radiation. Last two decades have seen a tremendous progress on passive radar, with several systems and prototypes built and proven at detecting targets of various types and at different ranges depending on the used waveforms [1]. However, research is still ongoing. The signal environment is constantly evolving and the update of the current broadcast and communication networks continuously offers new opportunities for innovative applications for this technology.

Most of the research activity in the field of passive radar focused on the possibility to detect, localize and track moving targets. Alongside the maturity level reached for these tasks, innovative techniques are being developed for advanced operational modes, such as inverse synthetic aperture radar (ISAR) processing [2], [3]. Several research efforts have been made to add passive ISAR capabilities to existing passive systems, mostly focusing on terrestrial transmitters of opportunity. FM signals have been considered

in [4] for cross-range profiling of aerial targets, while in the framework of short-range/indoor applications, Wi-Fi-based passive ISAR processing and experimental results have been provided in [5] and [6]. However, most of the open literature focuses on terrestrial TV signals operating in the UHF/VHF-band, due to their widespread availability and relatively high transmitted power, being the digital video broadcasting-terrestrial (DVB-T) the most considered option as adopted by most of the countries [7]–[11].

In parallel, the exploitation of satellite sources for passive radar applications begun to emerge. Traditionally regarded as inadequate due to their low power levels, such sources offer indeed interesting benefits with respect to their terrestrial counterparts. Satellites signals are less sensitive to multipath and shadowing effects, the transmitters are not vulnerable in situations of man-made or natural disasters and they can provide a much wider accessibility and coverage on the global scale. This latter characteristic is particularly attractive in maritime scenarios where the coverage offered by terrestrial sources is inherently limited, and recent works focused on ship target detection/localization with passive radar systems based on communication and navigation satellites [12]–[16]. Moreover, satellite-based passive ISAR has been addressed in [17] for the case of GNSS illuminators.

However, the most promising option for satellite-based passive imagery of ships seems the digital video broadcasting-satellite (DVB-S) [18]. Such signals are transmitted by satellites in geostationary orbits, therefore assure a permanent coverage over continental areas, even off-shore. Moreover, as the satellites keep nearly stated positions with respect to a generic point over the Earth' surface, reference signals can be captured via narrow beam antennas, allowing to steer a high-gain beam in the direction of the transmitter, making the direct channel less susceptible to interferences from multipath and other terrestrial RF sources. Ambiguity function has been found adequate for the passive radar use, with stable correlation properties [19]. Moreover, a relative wide bandwidth is available: DVB-S spectrum is densely populated by multiple transponders, each broadcasting signals over a bandwidth of tens of MHz, being 32 MHz the most common value. As the gaps between adjacent channels are relatively small, multiple transponders can be even combined to enhance the achievable range resolution. Noticeably, the system operates in the Ku-band, with carrier frequency in the range 10.7 GHz – 12.75 GHz, therefore having a high Doppler sensitivity and, thus, high cross-range resolution. Inspired by these potentialities, few recent studies investigated DVB-S-based passive ISAR at both the theoretical and experimental level [18], [20]–[24].

In this work, we investigate the possibility to exploit polarimetric data to enhance the quality of the DVB-S based passive ISAR imagery, with specific regard to ship targets. As a matter of fact, the possibility to exploit polarimetric data offers the opportunity to increase the target information space. As known, scattering mechanisms are sensitive to the polarization of the e.m. radiation, therefore target signatures can considerably vary with the polarization state of the signal potentially providing a richer set of features to characterize the image [25]. In the field of active radar imaging, several works investigated how to exploit Polarimetric ISAR (PolISAR) data for enhanced automatic target recognition (ATR) procedures [25]–[29]. Coming to the passive radar, few works considered the exploitation of polarization diversity to enhance the system performance [30], [31]; however, such works focused on the detection task while, at the best of our knowledge, open literature reports no investigations about passive PolISAR.

The exploitation of polarimetric data for passive ISAR purposes is indeed a very challenging objective. The first issue is due to the inherent bistatic nature of passive radar systems, which breaks the reciprocity between transmitter and receiver making the cross-polarized terms no longer equal, thus complicating the physical interpretation of the scattering matrices [32]–[34]. In addition, passive radars usually operate with two separated RF channels: one working with an antenna steered toward the opportunistic illuminator to record the direct signal (referred as to reference channel), and the other with the antenna pointed toward the surveyed area collecting the reflected signals to perform the radar tasks (surveillance channel). Therefore, the orientation of the polarization states of the direct/reflected waves differ. Furthermore, the user lacks the control over the transmitter power at the two polarizations.

Due to the above-mentioned issues, some adaptations must be made to enable polarimetric operations in the DVB-S-based passive ISAR framework. First, it should be noted that fully polarimetric radar systems usually transmit alternatively and receive simultaneously signals in the two orthogonal polarizations. A DVB-S satellite instead carries multiple transponders that are overlapped and interleaved in the horizontal and vertically polarization simultaneously [35]. Therefore, in our case, polarimetric operations are implemented by cross-correlating orthogonally polarized signals received at the reference and surveillance channel. Furthermore, it is necessary to refer to two different couples of orthogonal planes for the reference and surveillance channels. Indeed, even though differences in ionospheric propagation can be assumed negligible between the direct and reflected paths (due to their proximity), we must consider that the reference and surveillance acquisition chains use antennas differently oriented. Therefore, hereinafter we will refer to H_r, V_r and H_s, V_s for the horizontal/vertical signal states at the reference and surveillance channel, respectively. Moreover, as the power level over the horizontal and vertical antennas could differ, a lack of calibration between the polarimetric channels must be assumed.

In this work, aiming at exploiting the nice properties of DVB-S signals and adding polarimetric capabilities to the system despite the above limitations, we will investigate two main questions: 1) Can different scattering mechanisms, belonging to different parts of the imaged target, be separated in the polarimetric domain in the passive system? and 2) Is it possible to improve the reconstruction/extraction of the target shape/segment by fusing the polarimetric information?

To answer these questions, a dedicated experimental campaign has been conducted. The experimental hardware was the passive radar system SABBIA, developed at Fraunhofer FHR. Such system has been upgraded with respect to a first version [22] by adding one further channel, both for

the surveillance and the reference front-end, enabling the simultaneous reception of both horizontal/vertical polarized DVB-S signals. To focus on the polarimetric diversity and to effectively interpret the achieved results regardless inaccuracies due to data-driven motion compensation procedures, a cooperative target was involved equipped with an Inertial Measurement Unit (IMU) providing precise information on both target motion and attitude. This allowed us to produce images at the different polarimetric channels in a target fixed reference system via know-motion back-projection (KM-BP) algorithm. The images obtained at the different polarimetric channels have been then processed using different polarimetric tools to answer the questions above. Noticeably, as the target was yawing during the acquisition, images taken at a variety of target attitudes were at our disposal, offering us the chance to analyze results at different viewing angles.

One of the most used representations to discriminate among the different scattering mechanisms in the observed area relies on the Pauli's feature vector (PFV), as it is closely related to the physical properties of the target [36]. Another class of methods exploits the coherence/covariance matrix to provide a statistical description of the distributed scattering phenomenon; methods belonging to this class are the Entropy/Alpha (E^1/α) decomposition [37] and the Principal Component Analysis (PCA) [38], [39].

Another possibility is performing a multipolar data combination in the image domain. Algorithms belonging to this category give up distinguishing the scattering mechanisms occurring at the target, but rather they aim at combining the images at the different polarimetric channels on a pixel basis to achieve a new image of better quality. The underlying idea of such methods is that different polarization states may highlight some features of the target while suppressing others at the same time. One such an approach relies on the evaluation of the determinant of the Sinclair scattering matrix (det[S]), which is invariant to the polarization base in use and has been introduced in [34] as a feature for target classification. Another method belonging to this class is the Polarimetric Whitening Filter (PWF), introduced by Novak and Burl in [40] for optimum speckle reduction in polarimetric SAR. Such method requires only the knowledge of the polarimetric covariance of the disturbance background, namely it ignores the target contribution. Unlikely, the likelihood ratio test approach in [41] includes the target statistics in the polarimetric data model, showing that the best probability of target detection can be obtained via a weighted summation of the individual polarimetric channels. An approach along this line, but forcing to zero the polarimetric correlation of the target (since it can be spatially variant and difficult to be estimated), named Polarimetric Likelihood Ratio Test (P-LRT) has been here considered for combining the single polarimetric images into the optimum (in the likelihood ratio sense) image.

The six methods above, properly adapted to the passive case under consideration, have been applied to the experimental

data to conduct a polarimetric analysis of the ISAR images. Particularly, PFV, E/α and PCA have been considered to observe if different parts of the imaged target corresponding to different types of structure behave differently in the polarimetric domain, thus answering to question 1). Image domains methods, namely det[S], PWF, and P-LRT are instead suitable to answer question 2). (Some preliminary results considering PFV and det[S] based representations have been anticipated in [42].) Moreover, it is worth to point out that the latter approaches can be relevant in the case under consideration due to the restricted power budget, as the signal-to-noise ratio (SNR) of the resulting images can be reinforced.

The remainder of the paper is organized as follows. Section II details the experimental campaign and describes the processing scheme adopted to achieve multi-pol passive ISAR images. Section III defines the polarimetric tools considered for the analysis, whose experimental results are provided in Section IV. Conclusions and discussions about next stages of this research are given in Section V.

II. POLARIMETRIC DATA ACQUISITION

This section presents the polarimetric data acquisition campaign. First a short description of the receiving passive system and of the involved cooperative target is reported. Then, an overview of the applied signal processing is detailed followed by some preliminary experimental results.

A. Measurement Campaign

The trial took place during July 2018 alongside the Rhine river in Bonn, Germany. As passive radar, the DVB-S(2) based SABBIA system developed at Fraunhofer FHR was deployed. A picture of the two dish antennas, each connected to two identical receiver front-ends, one for surveillance and the other for reference, can be seen in Fig. 1. More details about the SABBIA system can be found in [22]. The main goal of this measurement campaign was to simultaneously acquire two orthogonal polarizations, therefore one further channel, both for the surveillance and the reference front-end, has been integrated to the system configuration described in [22]. As illuminator of opportunity the geostationary satellite ASTRA 1KR located at the 19.2° East orbital position [43], emitting signals in both polarizations within the Ku-band, has been exploited.

During the acquisitions, the signals have been collected with an instantaneous signal bandwidth of 80 MHz centered around 11347 MHz. The spectra of the reference signal for both the horizontal and vertical channel are shown in Fig. 2. As can be noted, we acquired a slightly more than two transponders in the horizontal case and about three transponders in the vertical case. Please note that the gaps between the DVB-S transponders do not produce any grating lobes inside the imaged area and do not significantly affect the pulse response in the range dimension, but simply create a slightly raised level of the sidelobes. For this reason, it is not necessary to include in the considered ISAR image formation technique any specific strategy to cope with gapped spectrum.

Fig. 3 shows the Königswinter ferry, involved in this campaign as a cooperative target. During the experiment an IMU

---

[1]The entropy has been indicated with the E to avoid the reader any confusion with the H used throughout the manuscript to indicate the horizontal polarization.

Fig. 1. DVB-S(2) based SABBIA system during the trial alongside the Rhine river in Bonn, Germany.
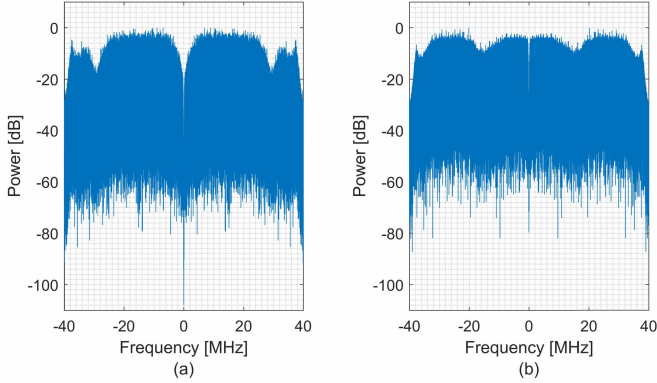

Fig. 2. Spectra of the reference signal: horizontal (a) and vertical (b) channel.

Fig. 3. Cooperative target: length L=46.24 m, width W=20 m. (Picture from Wikipedia.de, Wolkenkratzer 2015).

Fig. 4. Receiver trajectory in the target fixed system during 200 s observation time.

Fig. 5. Processing chain.

was placed on the target central superstructure to record both its motion and attitude.

In order to obtain ISAR images with several viewing angles, the cooperative target was intentionally yawing during the data recording. Fig. 4 shows the receiver trajectory in a target embedded system during the overall observation time of about 200 seconds. Here the blue rectangle represents a simplified target model comprising the four sides of the ferry, while the green line indicates the relative receiver motion that could be experienced supposing the target fixed.

B. Data Processing

The block diagram in Fig. 5 provides an overview of the basic processing steps applied to the acquired signals.
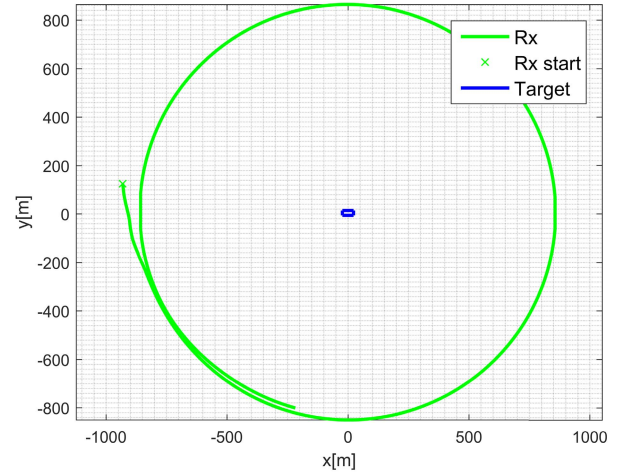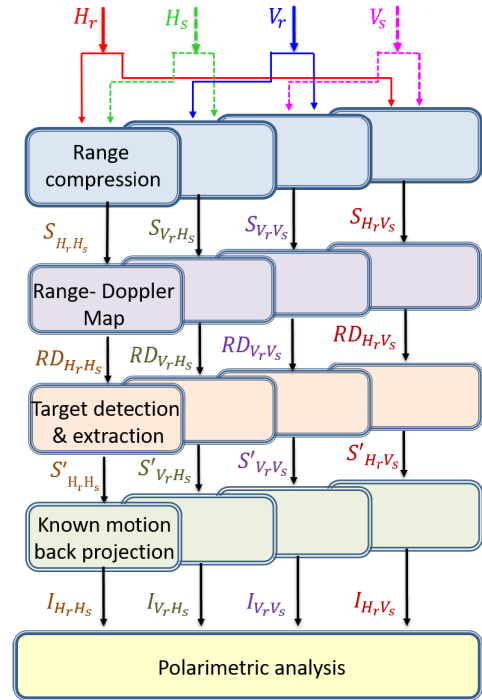
Two orthogonal polarizations, i.e. $\xi = \{H_r, V_r\}$, are acquired at the reference channel and two, i.e. $\chi = \{H_s, V_s\}$, at the surveillance one. DVB-S signals are continuous wave, so we assumed to perform a range compression over consecutive batches with constant duration T_{int} in order to define an equivalent (fast-time τ, slow-time t) domain. The range compression is obtained by cross-correlating the complex envelope of the signal received in the surveillance channel $\chi(t)$ with a replica of the transmitted signal $\xi(t)$, leading to the cross ambiguity function (CAF):

$$S_{\xi\chi}(\tau, f_D) = \int_{-\infty}^{+\infty} \xi(t) \cdot \chi^*(t - \tau) e^{-j2\pi f_D t} dt \quad (1)$$

where f_D is the bistatic Doppler. In digital processing, the ambiguity function can be approximated by the sum over N samples:

$$S_{\xi\chi}(\tau, f_D) = \sum_{n=0}^{N-1} \xi(nT_s) \cdot \chi^*(nT_s - \tau)e^{-j2\pi f_D nT_s/N} \quad (2)$$

where $T_s = f_s/N$, being f_s the sampling frequency, and N is the product of the Doppler bins number N_d and the range bins number N_r. The temporal integration interval is usually limited to the coherent integration time T_{int}. A reduction of the computational burden can be achieved by implementing the correlation in (2) in the frequency domain by means of a FFT. The Correlation FFT Algorithm [44] takes advantage of the fact that the samples along one Doppler bin are the cross-correlation between a Doppler shifted replica of the surveillance signal and the reference signal. This correlation becomes a multiplication in the frequency domain and the Doppler bin for the Doppler shift f_D can be calculated by

$$S(\tau)_{f_D} = IDFT\left\{\xi_{f_D}(k) \cdot \chi^*(k)\right\} \quad (3)$$

where * denotes the conjugation. In order to project the data from the (fast-time τ, Doppler f_D) domain to the (range r, Doppler f_D) domain, the electromagnetic wave propagation speed c has to be considered.

Then, the target of interest can be detected and the region of the Range- Doppler (RD) map containing it can be cropped for the following ISAR processing [3]. If necessary, the ISAR aperture time (i.e., the coherent processing interval CPI) can be extended by juxtaposing data corresponding to consecutive RD maps.

Each dataset is then processed exploiting a priori information regarding the target motion. The known motion back projection (KM-BP) algorithm introduced in [24] has been in this case applied to each polarization pair as follows

$$I_{\xi\chi}(x, y) = \sum_n S'_{\xi\chi}(f, t_n) \cdot e^{j2\pi f \frac{r_b(x,y,t_n)}{c}} \quad (4)$$

where (x, y) is a grid of points defined in the target fixed coordinate system, $S'_{\xi\chi}(f, t_n)$ is the range compressed signal in (fast frequency f, slow-time t) domain after the target extraction at the slow time instant $t_n \in CPI$ and r_b is the bistatic range retrieved from the IMU mounted on the target by considering the relative distances d between the transmitter T_x, the receiver R_x and the target T_g:

$$r_b(x, y, t_n) = d_{T_x T_g}(x, y, t_n) + d_{R_x T_g}(x, y, t_n) - d_{T_x R_x}(t_n) \quad (5)$$

Since the variations of the target attitude and the bistatic geometry make the image projection plane (IPP) changing with time, representing the images in a target embedded coordinate system might help in comparing ISAR products pertaining different time intervals.

Afterwards, the four polarimetric ISAR images as in (4) are used as input for the polarimetric analysis as detailed in Section III.
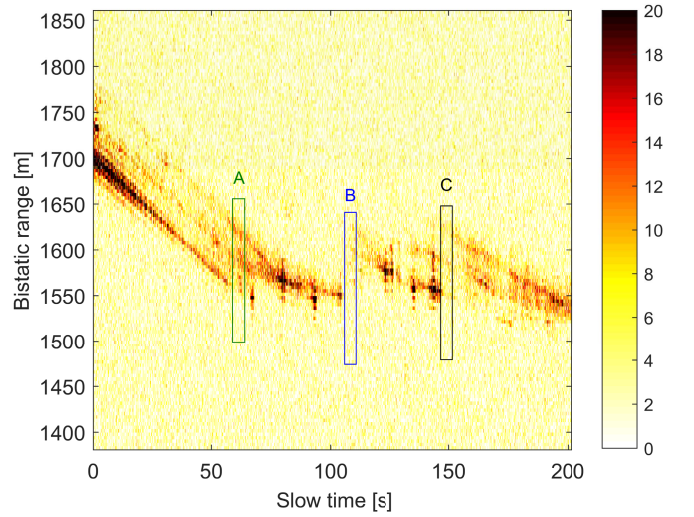

Fig. 6. $H_r H_s$-RPs over time [dB]. Data frames A, B, and C are highlighted as green, blue, and black boxes, respectively.

TABLE I
ANALYZED DATA

Frame	Starting time [s]	CPI [s]	Heading*[deg]	ω_z [deg/s]
A	60.4	0.8	[285.1, 286.6]	2
B	107.4	0.8	[92.2, 121.5]	4.9
C	147.6	0.8	[265.9, 267.8]	2.4

* beginning and end of the CPI

C. Single Polarization Experimental Images

Fig. 6 shows the collected radar data for the exemplary case of $H_r H_s$ polarization in terms of range profiles (RPs) in dB scale, normalized to the noise background, over the overall observation time interval of about 200 seconds. Shown data have been reformatted in a (range compressed, slow time) domain by using an equivalent pulse repetition frequency PRF = 1221 Hz. It is possible to observe that the SNR is considerably changing over time, mainly as a consequence of the change of the target orientation within the bistatic geometry (see Fig. 4). For the polarimetric analysis the three data frames A, B, and C highlighted in Fig. 6 with the green, blue and black boxes, respectively, have been selected. These frames have been selected considering different parameters, namely the SNR, the target rotation and the visibility of different scattering centers. Even though a higher SNR could permit us to better discriminate between target and background, in some frames the target rotation was not adequate for ISAR purposes. This was resulting in a single predominant scatterer (probably the central superstructure) masking other scattering points with lower RCS along the ferry. Therefore, we selected data frames showing both a sufficient SNR and a wide span of the target energy over multiple resolution cells.

For each analyzed data frame, Table I lists the respective starting time (with respect to the RPs of Fig. 6), CPI, heading and angular velocity ω_z values. The CPI has been selected as the maximum value for which the SNR of all the considered images shown a linear increase with the integration interval. While during the data acquisitions the heading presented
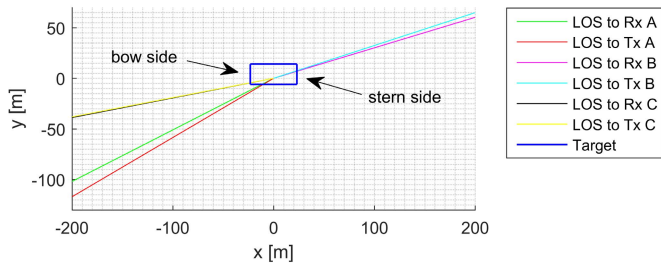
Fig. 7. Transmitter (Tx) and receiver (Rx) LOSs in the target fixed system for data frames A, B, and C.

an almost linear variation over time, the pitch and the roll angle variations were negligible thanks to the stability of the target on the river. Furthermore, also the total bistatic angle (accounting also for the elevation angle) showed a quite stable value around 30°. Taking into account the acquired signal bandwidth of 80 MHz and such bistatic angle value, a bistatic range resolution of about 3.88 m is obtained.

For the three analyzed time intervals, the experienced bistatic geometries can be projected on the target fixed coordinate system, as shown in Fig. 7. Here the ferry is depicted in blue, while the green, magenta and black solid lines indicate the target to receiver's line-of-sight (LOS) projections for the data frames A, B and C, respectively. The LOS from target to the transmitter for the data frames A, B and C are drawn with the red, cyan and yellow lines, respectively. Even if in the figure the geometry appears quasi-monostatic, we explicitly note that this sketched geometry only shows the projection onto the (x, y) plane, thus not accounting for the elevation angle.

With reference to data frame A, a yaw rate of about 2°/s was measured by the IMU (see Table I). From the bistatic geometry here experienced, we expect to observe the stronger returns from the bow and the side of the ferry which are in line-of-sight with the receiver.

In data frame B, the target rotated around itself of about 180° with respect to frame A, so that the opposite side of the ferry, which was shadowed before, might be now illuminated. The angular velocity measured during this acquisition is of about 4.9°/s, namely almost twice the value pertaining frame A.

Finally, when the data frame C is considered, the cooperative ferry rotated almost 360° around itself with respect to the data frame A. In this case a slightly different yaw rate (about 2.4°/s) and bistatic geometry are experienced with respect to data frame A. As for frame A, we expect to see the stronger scattering from the bow of the ferry.

Fig. 8 shows the $H_r H_s$ - RD map pertaining frame A in dB scale, where 0 dB denotes the noise background. Here the analyzed CPI of about 0.8 s, together with the yaw rate of about 2°/s, is resulting in a bistatic cross-range resolution approximately equal to 0.50 m. Inspecting the enlargement of the sub-image highlighted with the green box, we can notice that the target is approaching to the receiver showing a positive Doppler frequency between 40 Hz and 110 Hz. At bistatic range of around 1900 m and bistatic Doppler frequency equal
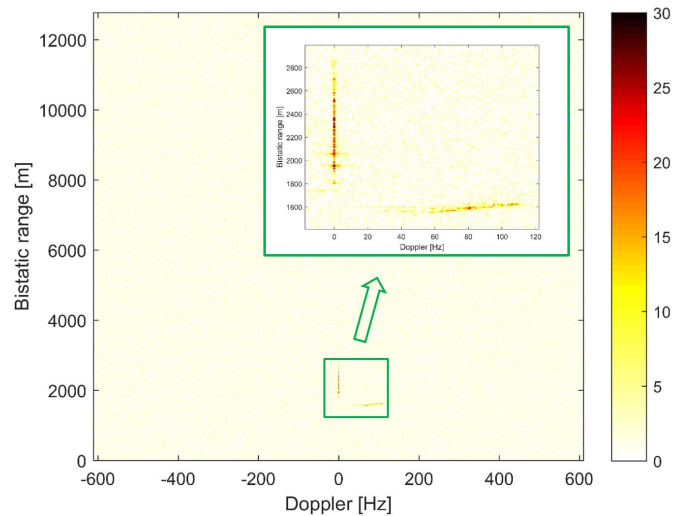

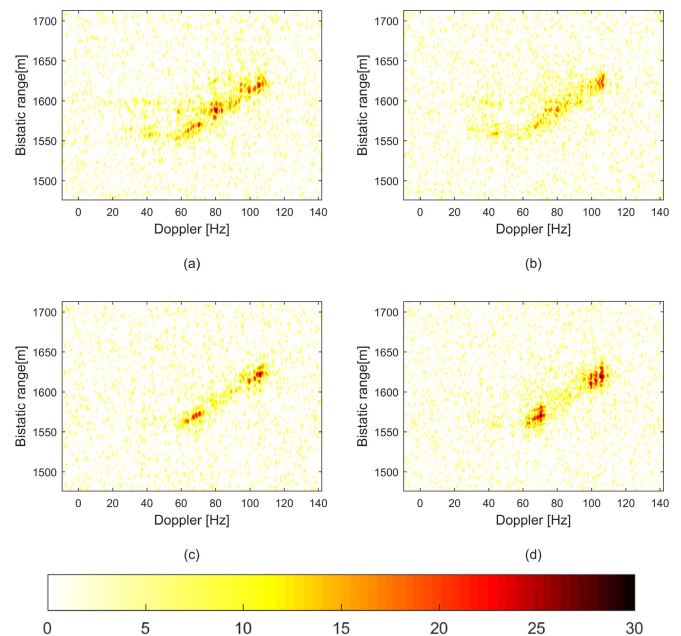Fig. 8. Data frame A - $H_r H_s$ RD map [dB] before the target extraction.

Fig. 9. Data frame A - RD maps [dB]: (a) $H_r H_s$, (b) $V_r V_s$, (c) $H_r V_s$, (d) $V_r H_s$.

to 0 Hz, the stationary return coming from various structures and objects located on the opposite side of the river can be clearly recognized. After the target detection and extraction, we obtain the four polarimetric RD images in Fig. 9, where we can recognize how in each image different portions of the ferry give rise to distinct bright returns. Recalling the resolution cell of about 3.88 m × 0.50 m in the (range, cross-range) plane and the ferry size of about 46 m × 20 m, we observe as expected multiple scatterers in both the directions.

The corresponding KM-BP radar images for each polarization pair are depicted in Fig. 10, where 0 dB denotes the mean background power. The superimposed blue rectangle represents a simplified target model comprising the four sides of the ferry, while the blue star denotes the position of the IMU on the central superstructure. We can notice how target imaging via BP in the target fixed coordinate
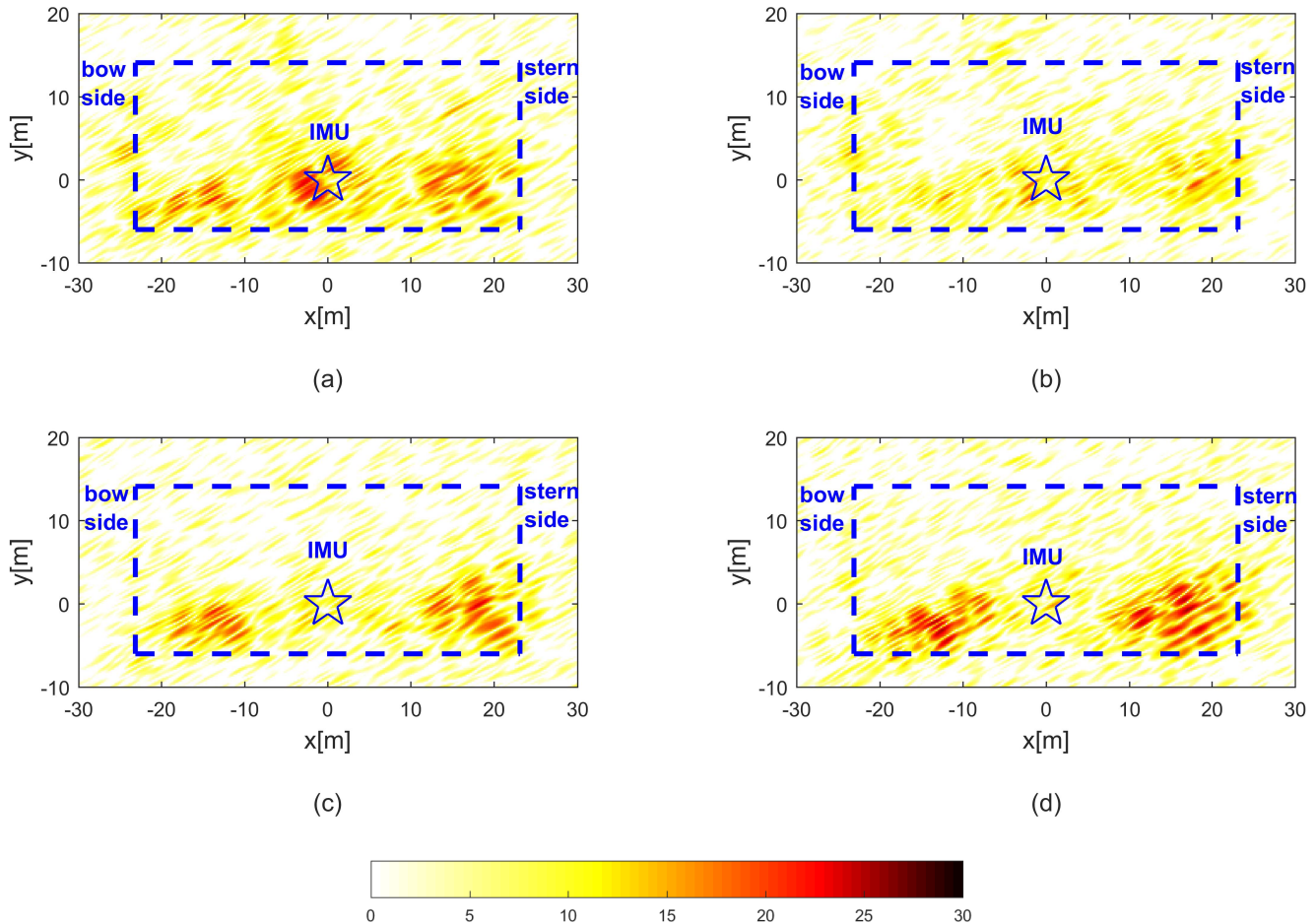
Fig. 10. Data frame A - BP maps [dB]: (a) $H_r H_s$, (b) $V_r V_s$, (c) $H_r V_s$, (d) $V_r H_s$. The bow, IMU and stern positions here explicitly indicated are valid for all the following BP maps.

system simplifies the comparison between different ISAR products, allowing us to better recognize the target scatterers in each image. As expected from the bistatic geometry in Fig. 7, all images show a strong signal scattered from the bow and from the illuminated side of the ferry (namely, at negative values of y-axis). Nevertheless, each polarimetric channel clearly highlights different scattering centers. While in the $H_r H_s$ image [Fig. 10 (a)] a bright return is coming from the central superstructure where the IMU was placed, the $V_r V_s$ image [Fig. 10 (b)] appears more homogeneous and less strong scatterers can be recognized. Finally, the $H_r V_s$ [Fig. 10 (c)] and $V_r H_s$ [Fig. 10 (d)] images present similar stronger scattering behaviors in correspondence of the ferry deck. It is worth noticing that due to the bistatic geometry (and the consequent lack of validity of the reciprocity theorem [32]), the two cross-polarized ISAR images $H_r V_s$ and $V_r H_s$, although similar, are indeed not identical. Unlikely we did not collect detailed information about the cars on board of the ferry during the acquisitions.

The SNR values (in dB) of the KM-BP images, for each analyzed data frame and for each polarization pair, can be found in Table II: we observe the considerably lower SNR values pertaining frame B with respect to frames A and C that allow us to investigate the improvement arising from the

TABLE II
SNR [dB]

Frame	$H_r H_s$	$V_r V_s$	$H_r V_s$	$V_r H_s$
A	16.12	12.20	16.54	18.48
B	8.12	12.81	4.80	9.11
C	13.64	11.53	10.58	18.94

exploitation of polarimetric diversity in both medium and poor SNR conditions. These ISAR products are then fed in input to the polarimetric analysis stage, as detailed in Section III.

III. PASSIVE POLARIMETRIC ISAR ALGORITHMS

The polarimetric data are usually represented by means of the scattering or Sinclair matrix, [36], which in our case can be defined as

$$S_m = \begin{bmatrix} I_{H_r H_s} & I_{V_r H_s} \\ I_{H_r V_s} & I_{V_r V_s} \end{bmatrix} \qquad (6)$$

where for simplicity the dependency on (x, y) has been omitted.

In order to extract the information from polarimetric ISAR data, in this work we will consider different approaches, which resemble complementary information that can be extracted from polarimetric analysis. Specifically, Pauli's Feature Vector

and bistatic polarimetric feature-based methods (Sec. III-A and Sec. III-B, respectively) aim at discriminating among different scattering phenomenon in the target region. These approaches are well suited for high-SNR scenarios, where the polarimetric information can be exploited to identify the different scattering mechanisms. On the other hand, the image domain algorithms (Sec. III-C) seek to enhance the reconstruction capability of the target shape. These latter approaches are more suited in low-SNR scenarios, where polarimetry can be conveniently exploited to enhance target visibility.

A. Decomposition to Pauli's Feature Vector-Elements

The most commonly known and applied polarimetric decomposition is the Pauli decomposition. In the monostatic case, radar images are often represented by means of three images that are the results of the projection of the scattering matrix onto the Pauli basis [36] for each image pixel. Such three images are usually combined together to obtain a single RGB image. As in the bistatic case $I_{H_r V_s} \neq I_{V_r H_s}$ the Pauli's feature vector (PFV) is four-dimensional. Considering the adaptation for the passive case, the (modified) PFV is given by

$$\mathbf{k}_{4P} = \begin{bmatrix} I_{H_r H_s} + I_{V_r V_s} \\ I_{H_r H_s} - I_{V_r V_s} \\ I_{H_r V_s} + I_{V_r H_s} \\ j(I_{H_r V_s} - I_{V_r H_s}) \end{bmatrix} \tag{7}$$

In order to exploit all the polarimetric information available in our case and to simultaneously enable an RGB representation, we can use the first three vector components to obtain a color coded image. In particular, we will consider the following association: Red = $|I_{H_r H_s} - I_{V_r V_s}|$; Green = $|I_{H_r V_s} + I_{V_r H_s}|$; and Blue = $|I_{H_r H_s} + I_{V_r V_s}|$.

B. Bistatic Polarimetric Features

The aim of the bistatic polarimetric features techniques is to highlight the different polarimetric scattering mechanisms as observed into the different polarimetric ISAR products by resorting to statistical descriptions of the distributed scattering. To this end, we will consider two well-known methods, namely (a) the entropy and mean alpha angle decomposition [37], and (b) the principal component analysis [38]. To be noticed that the use of two different decompositions in the same class (i.e., decompositions aimed at extracting polarimetric features) allows us also to crosscheck the obtained results, indirectly confirming their validity.

1) Polarimetric Entropy and Mean Alpha Angle: In cases dealing with the statistics of fluctuating targets, the coherence matrix is usually exploited [36]. In the bistatic case we consider a [4×4] coherence matrix defined as

$$T_4 = \langle \mathbf{k}_{4P} \cdot \mathbf{k}_{4P}^{\dagger} \rangle \tag{8}$$

$\dagger$ denotes the Hermitian operator and $\langle * \rangle$ indicates spatial averaging; therefore, T_4 is obtained by averaging, over a proper support region, the outer product of the bistatic Pauli vector $\mathbf{k}_{4P}$ defined in (7) for each image pixel.

Being Hermitian positive semidefinite, T_4 can be unitarily diagonalized by a unitary matrix with nonnegative eigenvalues λ_i

$$U^{-1} T_4 U = \Lambda = diag[\lambda_1, \lambda_2, \lambda_3, \lambda_4] \tag{9}$$

where $U = [\hat{\mathbf{u}}_1, \hat{\mathbf{u}}_2, \hat{\mathbf{u}}_3, \hat{\mathbf{u}}_4]$ is the matrix of the corresponding eigenvectors.

The polarimetric entropy E, which measures the randomness of the scattering process, is calculated as

$$E = -\sum_{i=1}^{4} P_i log_4(P_i) \tag{10}$$

where $P_i = \lambda_i / \sum_{k=1}^{4} \lambda_k$ are the probabilities obtained from the eigenvalues λ_i of T_4. The polarimetric entropy values are comprised between 0 and 1: for smooth surfaces, E tends to zero implying a non-depolarizing scattering process described by a single scattering matrix, while it increases with surface roughness (depolarizing surfaces).

The mean α angle is defined as

$$\alpha = \sum_{i=1}^{4} P_i \alpha_i \tag{11}$$

where $\alpha_i = arccos(|\hat{\mathbf{u}}_i|)$ is the angle representing the polarimetric behavior of the i-th eigenvalue. The angle α usually indicates the type of the mean scattering process occurring, like surface, volume or double bounce scattering.

2) Principal Component Analyisis: Let

$$C_4 = \langle \mathbf{k}_{4L} \cdot \mathbf{k}_{4L}^{\dagger} \rangle \tag{12}$$

be the [4×4] covariance matrix, which is obtained by averaging of the outer product of the so-called lexicographic vector $\mathbf{k}_{4L}$ defined as

$$\mathbf{k}_{4L} = \begin{bmatrix} I_{H_r H_s} \\ I_{V_r H_s} \\ I_{H_r V_s} \\ I_{V_r V_s} \end{bmatrix} \tag{13}$$

As for the coherence matrix, also the covariance matrix can be unitarily diagonalized by a unitary matrix with nonnegative eigenvalues

$$V^{-1} C_4 V = \Sigma = diag[\sigma_1, \sigma_2, \sigma_3, \sigma_4] \tag{14}$$

where $V = [\hat{\mathbf{v}}_1, \hat{\mathbf{v}}_2, \hat{\mathbf{v}}_3, \hat{\mathbf{v}}_4]$ is the matrix of the eigenvectors and $\sigma_1 \geq \sigma_2 \geq \sigma_3 \geq \sigma_4 \geq 0$ are the corresponding eigenvalues.

A new target feature vector z can be introduced considering the following linear transformation

$$\mathbf{z} = \begin{bmatrix} z_1 \\ z_2 \\ z_3 \\ z_4 \end{bmatrix} = V^{\dagger} \cdot \mathbf{k}_{4L} = \begin{bmatrix} \mathbf{v}^{\dagger}_1 \cdot \mathbf{k}_{4L} \\ \mathbf{v}^{\dagger}_2 \cdot \mathbf{k}_{4L} \\ \mathbf{v}^{\dagger}_3 \cdot \mathbf{k}_{4L} \\ \mathbf{v}^{\dagger}_4 \cdot \mathbf{k}_{4L} \end{bmatrix} \tag{15}$$

which is equivalent to

$$\mathbf{k}_{4L} = V \cdot \mathbf{z} \tag{16}$$

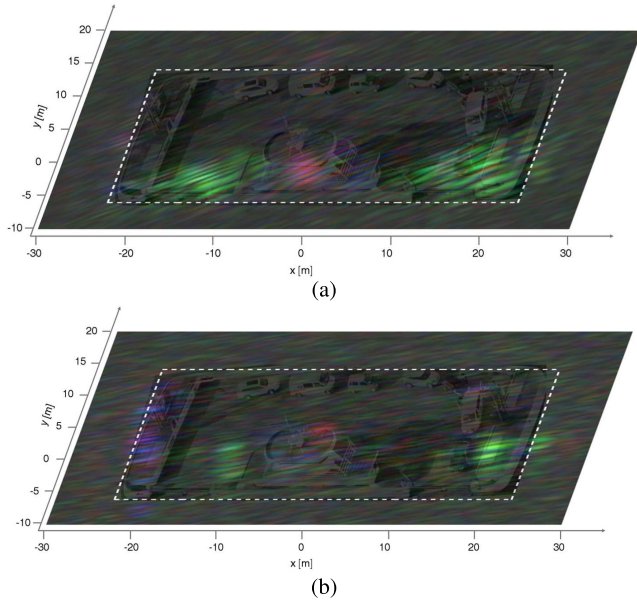The components $z_i (i = 1, ..4)$, known as principle components, are uncorrelated orthonormal random variables whose

Fig. 11. Modified Pauli Decomposition: Red $= |I_{H_r H_s} - I_{V_r V_s}|$; Green $= |I_{H_r V_s} + I_{V_r H_s}|$; and Blue $= |I_{H_r H_s} + I_{V_r V_s}|$ for data frame A (a) and data frame C (b).
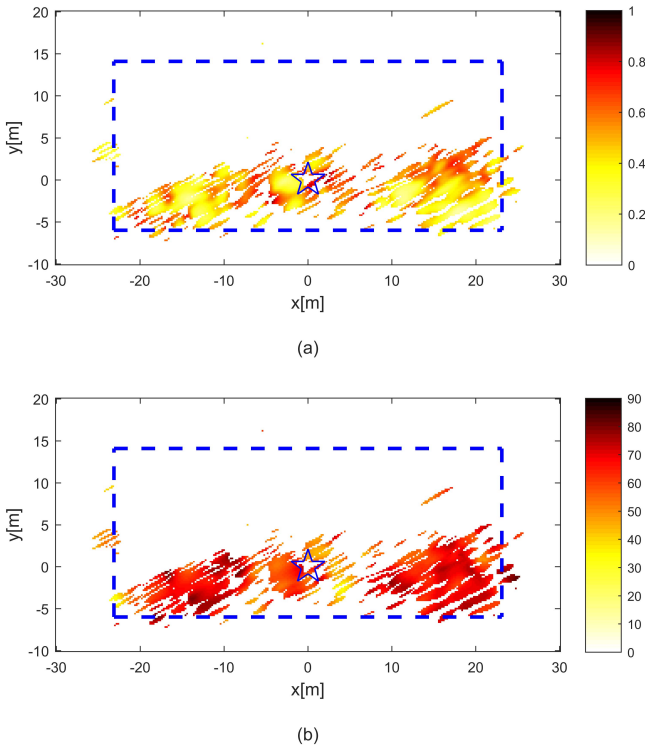

Fig. 12. Entropy in linear scale (a) and α angle in degrees (b) for data frame A. Only values are shown for those pixels having an $SNR > 13$ dB in at least one polarimetric ISAR image (see Fig. 10).

variances are equal to the corresponding eigenvalues of C_4. The scattering matrix (6) can be then expanded into four uncorrelated point targets formed by the loading matrices with random coefficients z_i

$$S_m = \sum_{i=1}^{4} z_i \begin{bmatrix} v_{i1} & v_{i3} \\ v_{i2} & v_{i4} \end{bmatrix} = \sum_{i=1}^{4} z_i S_i \qquad (17)$$
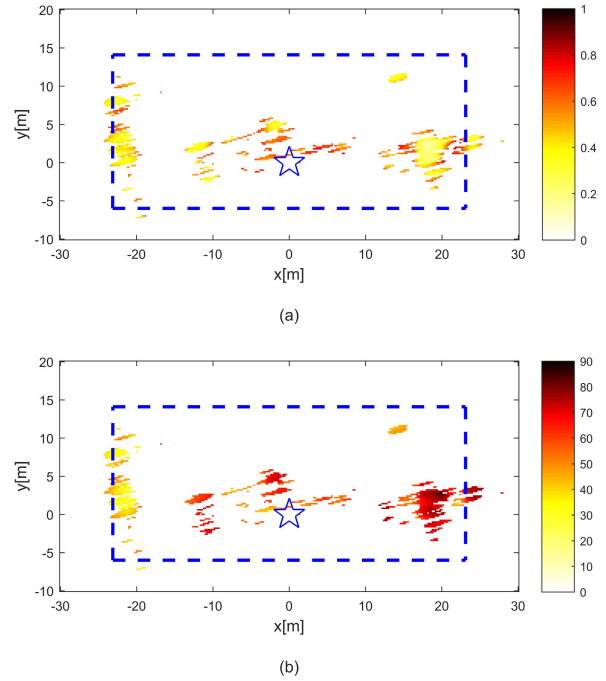

Fig. 13. Entropy in linear scale (a) and α angle in degrees (b) for data frame C (threshold $= 13$ dB).
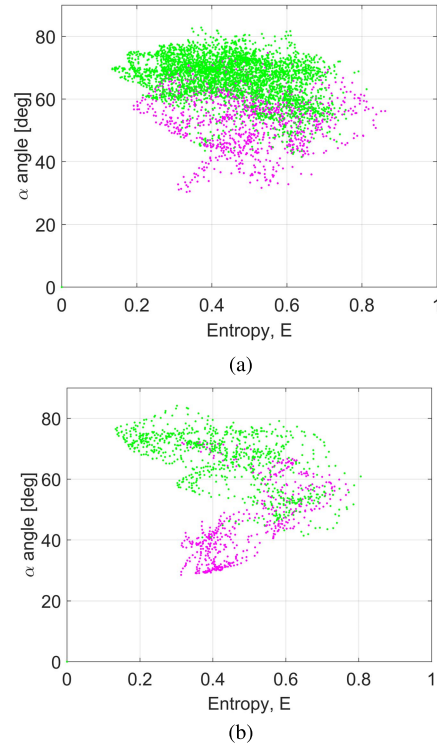

Fig. 14. E/α plane: (a) frame A, (b) frame C.

C. Image Domain Techniques

In the category of image domain techniques, we consider three different approaches whose aim is to combine the different polarimetric ISAR images into one single ISAR product where possibly all information is condensed. This might be for instance helpful in low SNR regimes, where the polarimetric diversity is simply exploited to increase the final SNR in the
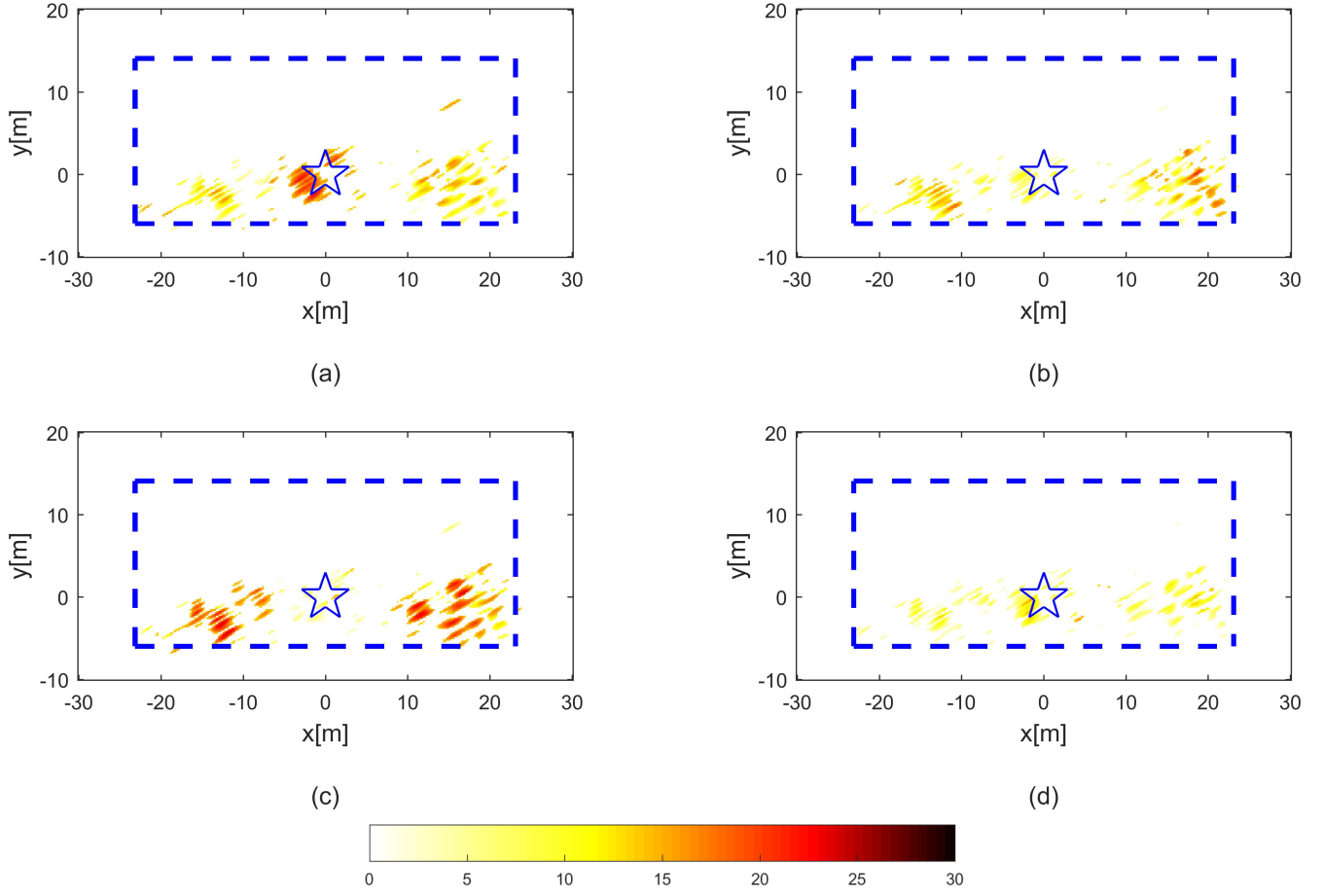
Fig. 15. PCA data frame A ($z_1 v_{1i} > 13$ dB, $i = 1, \ldots, 4$): (a) $z_1 v_{11}$, (b) $z_1 v_{12}$, (c) $z_1 v_{13}$, (d) $z_1 v_{14}$.

ISAR product. The image domain techniques here considered are: (i) determinant of the Sinclair matrix, as proposed in [34]; (ii) polarimetric whitening filter [40]; and (iii) polarimetric likelihood ratio test [41].

1) Determinant as a Feature: The determinant of the Sinclair matrix, which is invariant to the polarization bases in use [34], is here introduced to obtain a new ISAR product as

$$I_{det} = det[S_m] \qquad (18)$$

where the value of each pixel is related to the polarimetric information retrieved from all the channels.

2) Polarimetric Whitening Filter: The Polarimetric Whitening Filter (PWF) [40] produces a minimum-speckle image by combining the complex elements of the scattering matrix exploiting the covariance matrix $C_{4,n}$ defined as in (12) and calculated over an image region containing background only. The filtered image is given by

$$I_{PWF} = \mathbf{k}_{4L}{}^{\dagger} C_{4,n}^{-1} \mathbf{k}_{4L} \qquad (19)$$

3) Polarimetric Likelihood Ratio Test: The third considered technique is the polarimetric likelihood ratio test (P-LRT). In the case of noise versus target plus noise scenario, the P-LRT takes the form [41]

$$\mathbf{k}_{4L}{}^{\dagger} (C_{4,n}^{-1} - C_{4,n+t}^{-1}) \mathbf{k}_{4L} \qquad (20)$$

where $C_{4,n+t}$ is the target plus noise covariance matrix. Here we assume negligible the correlation among the different polarimetric channels for both the disturbance background and the target components. Such assumption is motivated by the low correlation levels observed in the considered experimental datasets for the background and by the highly spatially variant behavior of the target that makes the estimation very difficult in practice. On this basis, it could be shown ([16]) that (20) takes the form

$$I_{P-LRT} = \sum_{\xi\chi} w_{\xi\chi} |I_{\xi\chi}|^2 \qquad (21)$$

where $\xi = \{H_r, V_r\}$, $\chi = \{H_s, V_s\}$ and $w_{\xi\chi} = SNR_{\xi\chi}(x, y)/(SNR_{\xi\chi}(x, y) + 1)$ being $SNR_{\xi\chi}$ the local SNR value at image $I_{\xi\chi}$. Namely, for each pixel of the I_{P-LRT} image, the local level of SNR is measured and used to weight the contribution of the single polarimetric BP image in the final product.

It is worth to note that both the PWF and the P-LRT specifically aim at improving the poor received target signal level, which is a typical condition when geostationary illumination is exploited.

IV. Experimental Multipolar Images

This Section presents the results obtained by applying the polarimetric analysis techniques introduced in Section III to the experimental data described in Section II.
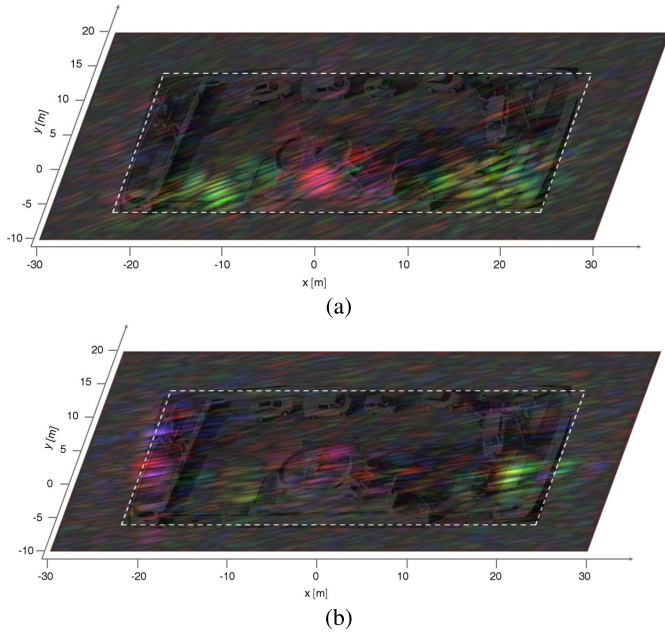
Fig. 16. RGB image PCA analysis: (a) frame A, (b) frame C.

Fig. 17. PCA 3-D plot: (a) frame A, (b) frame C.

First, a comparison between data frames A and C (characterized at the single polarimetric channel level by a higher SNR value, see Table II) will be illustrated applying the modified Pauli decomposition and the bistatic polarimetric features extraction introduced in Section III.A and Section III.B, respectively. Afterwards, image domain algorithms will be applied to data frame B, which shows significantly lower SNR values with respect to other data frames.

A. Decomposition to Pauli's Feature Vector-Elements

Fig. 11 shows the results obtained by applying the modified Pauli decomposition to both data frame A [Fig. 11 (a)] and C [Fig. 11 (b)], where the red, green and blue colors are related to the first three elements of the PFV $\mathbf{k}_{4P}$. In the figure, the results from the Pauli decomposition are overlapped to a top view of the involved target. Considering data frame A, we can nicely distinguish two lateral scattering spots, where the green color is brighter (i.e., a considerable contribution is provided by the cross-polar channels), from the central one, where red and blue are predominant (i.e. co-polar returns are dominant). The evident symmetry of the scattering mechanisms can be related to the symmetry of the target itself (see Fig. 10 and Fig. 3) and to the specific illumination geometry.

With respect to data frame C, we expect to see a stronger signal scattered from the bow of the ferry (see Fig. 7) and this is confirmed from the modified Pauli representation [Fig. 11 (b)]. It can also be noticed that the scattering from the border can be related to the co-polar channels (red and blue colors) as that one from the superstructure, while the cross-polar components are stronger on the lateral spots as for the data frame A. The symmetry of the scattering mechanisms is less evident in data frame C than data frame A, probably because here the angle of view is more oriented toward the bow of the ferry and different scattering mechanisms between
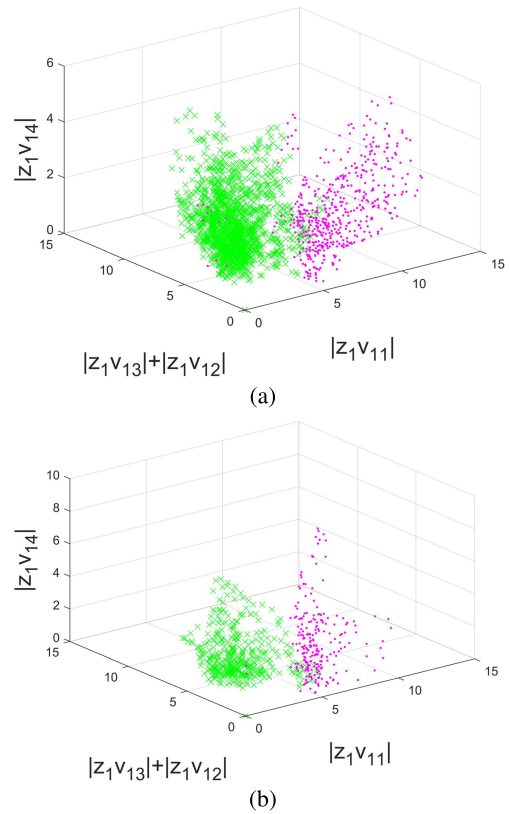
bow and stern can be experienced. In both cases, the pixel colors are varying mostly with respect to its position along the x-axis. We can recognize that within the two intervals [-26 m, 20 m] and [-5 m, 5 m] along the x-axis, red and blue colors, both related to the co-polar channels, are predominant; while for x-axis values within the intervals [-20 m, -5 m] and [5 m, 26 m], most of the pixels are green because in this case a stronger scattering is coming from the cross-polar channels.

B. Bistatic Polarimetric Features

Fig. 12 shows the entropy and α angle calculated for data frame A. A window size of 7×7 pixels was chosen to average the coherence matrix (8). For the sake of clearness of the representation, E and α values have been calculated only for those points where at least one of the four BP-images presents an SNR value above 13 dB (see Fig. 10). For data frame A, low entropy values, related to a stable scattering behavior, can be mainly recognized. The α angle values lay between $40°$ and $80°$, thus suggesting volume scattering mechanisms for the central superstructure and double bounce for the ferry deck.

Regarding data frame C (Fig. 13), the entropy image shows a noisier behavior of the scattering mechanisms at and around the central superstructure. This could be related to the different angle of view experienced in this case.

Furthermore, along the ferry bow (negative values of x-axis), which in this case is facing directly the passive receiver, lower α values suggest a surface scattering mechanism.
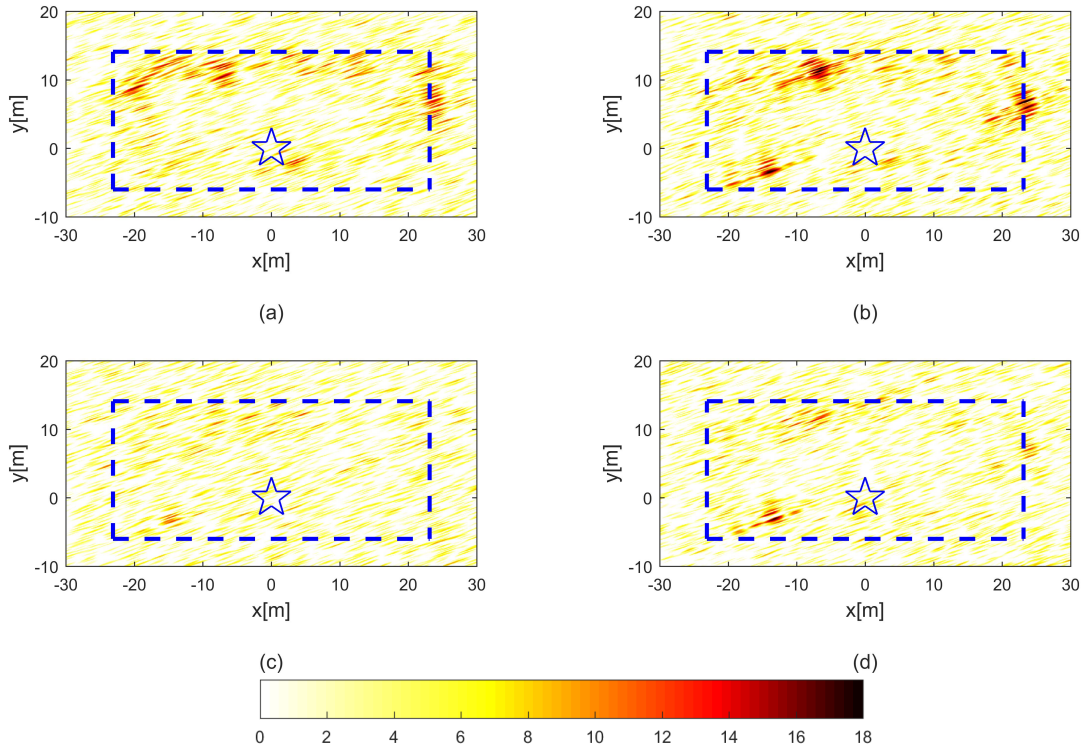
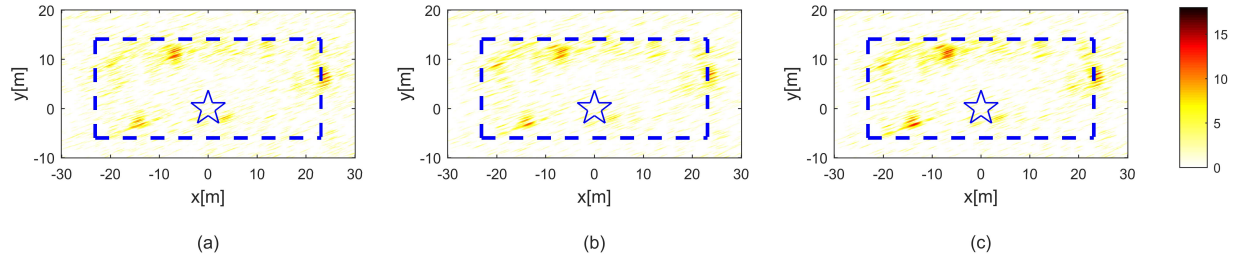Fig. 18. Data frame B - BP maps [dB]: (a) $H_r H_s$, (b) $V_r V_s$, (c) $H_r V_s$, (d) $V_r H_s$.

Fig. 19. Multi-pol. ISAR images data frame B − (a) I_{det}, (b) I_{PWF}, and (c) $I_{P\text{-}LRT}$.

Fig. 14 shows a comparison between frames A and C in the (E/α) - plane. Recalling the pixel colors variation along the x-axis and its association to the co-polar or cross-polar channels stressed in Section IV.A, we separate the image pixels in the (E/α) - plane in two groups. The former, related to the co-polar channels and pertaining the two intervals $x \in$ [-26 m, 20 m] and $x \in$ [-5 m, 5 m] is represented by magenta markers, whereas the latter, corresponding to the cross-polar channels and pertaining the two intervals $x \in$ [-20 m, -5 m] and $x \in$ [5 m, 26 m], is depicted in green.

From this representation, we can notice how the E values are almost homogeneously concentrated within the [0.2, 0.8] values in both cases, while the green pixels are mostly related to larger α angle values with respect to the magenta ones, thus indirectly confirming results observed with the Pauli decomposition.

Anyway, we have to stress that the rigorous distinction between the scattering mechanisms by means of the entropy and mean α angle has been proved in the literature mostly in the monostatic case contemplating natural areas [37]. Therefore, further investigations should be done to confirm the validity of these approaches in our case of study.

For the Principal Component Analysis, a window size of 5×5 pixels was used to obtain the covariance matrix (12). In this work, we will concentrate on the principle component with the highest variance, thus one matrix of the four possible matrices in Fig. 15 will be used in order to generate the images. The resulting images for frame A are depicted in dB scale in Fig. 15, where a similar thresholding as before has been applied to only retain pixels with sufficient SNR. We can clearly see how, for each component, different target features are more or less bright.

Furthermore, if we compare the retrieved images with the original ones in Fig. 10, a similarity among the couples $(I_{H_r H_s}, z_1 \ v_{11})$, $(I_{H_r V_s}, z_1 \ v_{12})$, $(I_{V_r H_s}, z_1 \ v_{13})$, $(I_{V_r V_s}, z_1 \ v_{14})$ can be noted, suggesting that, even without calibration, the collected polarimetric channels are almost uncorrelated and orthonormal. To better visualize these similarities, Fig. 16 shows the RGB images superimposed to the ferry optical photograph after the PCA for frames A and C, where the similarities with the images in Fig. 10 can be clearly recognized. Finally, Fig. 17 depicts the image pixel values in a 3-D plot where $|z_1 \ v_{11}|$, $|z_1 \ v_{12} + z_1 \ v_{13}|$, and $|z_1 \ v_{14}|$ represent the three axes. As for the (E/α) - plane (Fig. 14), the magenta and
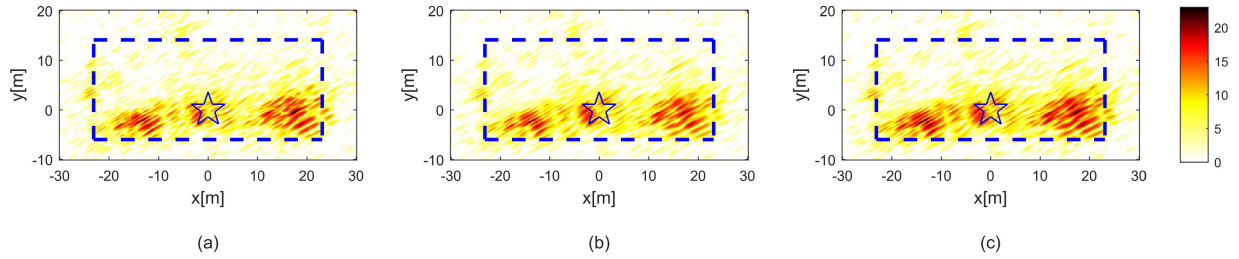
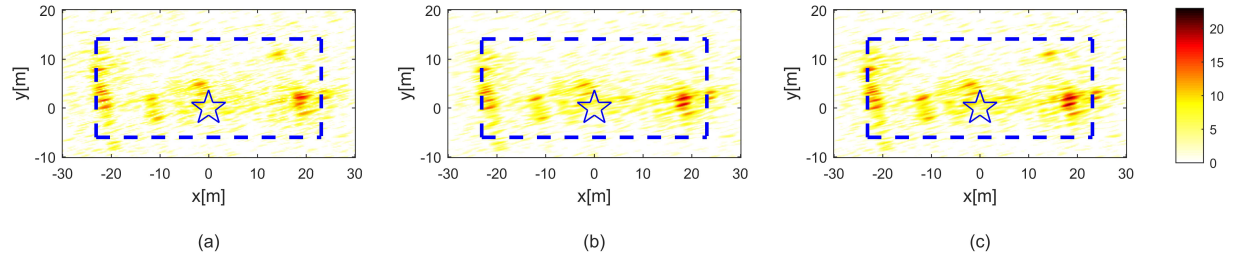Fig. 20. Multi-pol. ISAR images data frame A – (a) I_{det}, (b) I_{PWF}, and (c) I_{P-LRT}.

Fig. 21. Multi-pol. ISAR images data frame C – (a) I_{det}, (b) I_{PWF}, and (c) I_{P-LRT}.

green colors are associated to the image pixel position along the x-axis. In these plots we can clearly see how the pixels associated to different colors are grouped in two different areas in both the analyzed frames. This behavior, in agreement with the behavior observed in the (E/α) - plane, indirectly confirms the validity of the achieved results and highlights how different scattering mechanisms in different parts of the same target behave differently in the polarimetric domain.

C. Image Domain Techniques

As already mentioned, data frame B presents a different angle of view with respect to frames A and C. This might permit us to visualize the side of the ferry, which was shadowed in the two datasets analyzed till now. Unfortunately, this frame presents a low SNR as can be noted in Fig. 18, especially for the cross-polarized channels. This behavior might be due to the different view angles likely causing a less favorable radar cross section. In addition, we have to observe that during the CPI of about 0.8 s, a greater variation of the scattering behavior for each reflecting point is expected, which might lead to a lower integration gain. In order to cope with such low SNR conditions, the three different image domain algorithms introduced in Sec. III.C, are here taken into account.

Fig. 19 shows the multipolar images obtained applying the $det(S_m)$, the PWF and the P-LRT to data frame B. We can see how the image domain algorithms actually minimize the noisy background with respect to single polarization images. Therefore, we can better recognize the target features along the opposite side of the ferry, which is in this case in line-of-sight with the passive receiver, and on the upper part of the stern.

For the sake of completion, in Figs. 20 - 21 the results retrieved for the data frames A and C are depicted. It can be here observed as the fusion of the polarimetric information allows to clearly recognize and extract the bow, the bottom part of the deck and the central superstructure.

TABLE III
IMAGE CONTRAST AND ENTROPY VALUES

Frame	Intensity Contrast			Entropy		
	I_{det}	I_{PWF}	I_{P-LRT}	I_{det}	I_{PWF}	I_{P-LRT}
A	2.27	2.05	2.25	9.73	9.83	9.67
B	1.00	0.90	1.18	11.79	11.85	11.73
C	1.51	1.73	1.95	10.17	10.16	10.03

Table III lists the image contrast and entropy values for each data frame obtained via the different image domain techniques. As can be noted, the P-LRT is providing the best trade-off between high contrast and low entropy for all the data frames. Finally, it is worth to notice that the fusion of the multi-angle information, in addition to the multipolar data combination, could allow the retrieval of the complete target shape, enhancing the classification capability of the system [45], which will be subject for future investigations.

V. CONCLUSION

In this work, we have investigated and demonstrated the potentialities of polarimetric diversity for passive ISAR imaging. To this purpose, an experimental campaign has been carried out exploiting DVB-S(2) illuminators of opportunity and several polarimetric data sets with distinct bistatic geometries have been considered. To obtain the focused ISAR products in a common target fixed plane by means of a BP algorithm, we took advantage of the known motion information of a cooperative ferry. Then different approaches in the polarimetric domain have been applied to the retrieved ISAR images. The Pauli Decomposition has been adapted to the bistatic case and represented in a color coding in order to associate distinct structures within the imaged target to the co-polar or the cross-polar channels, respectively. Then, two bistatic polarimetric features techniques, namely the entropy and mean alpha angle decomposition and the principal component analysis, have been applied to the data. With both the techniques, similar results concerning the different polarimetric scattering

mechanisms arising from distinct parts of the same target have been retrieved. Such polarimetric diversity could enable in future new ship classification methods exploiting passive bistatic systems.

As in the passive environment a lower power budget with respect to the active case is expected, the polarimetric information might be also exploited to increase the final SNR in the ISAR image. To this aim, three different image domain techniques (the determinant of the Sinclair matrix, the polarimetric whitening filter and the likelihood ratio test) have been applied to the considered data sets. Such techniques have been shown suitable to improve the separation between the noisy background and the imaged target with respect to single polarization case, permitting us to better recognize the target features/shape. The P-LRT, in particular, is providing the best trade-off between high contrast and low entropy for all the considered data frames.

Even if the challenging passive radar environment required the exploitation of controlled experiments to make possible this work, the achieved results have demonstrated that the multipolar data can enable both the recognition of different scattering mechanisms within the imaged target and the passive image quality improvement. Of course, further research efforts and experiments are required to generalize this first analysis.

ACKNOWLEDGMENT

REFERENCES

[1] H. Griffith and C. J. Baker, *An Introduction to Passive Radar*. Norwood, MA, USA: Artech House, 2017.

[2] M. Martorella and E. Giusti, "Theoretical foundation of passive bistatic ISAR imaging," *IEEE Trans. Aerosp. Electron. Syst.*, vol. 50, no. 3, pp. 1647–1659, Jul. 2014.

[3] J. L. Garry and G. E. Smith, "Passive ISAR part I: Framework and considerations," *IET Radar, Sonar Navigat.*, vol. 13, no. 2, pp. 169–180, Feb. 2019.

[4] F. Colone, D. Pastina, and V. Marongiu, "VHF cross-range profiling of aerial targets via passive ISAR: Signal processing schemes and experimental results," *IEEE Trans. Aerosp. Electron. Syst.*, vol. 53, no. 1, pp. 218–235, Feb. 2017.

[5] F. Colone, D. Pastina, P. Falcone, and P. Lombardo, "WiFi-based passive ISAR for high-resolution cross-range profiling of moving targets," *IEEE Trans. Geosci. Remote Sens.*, vol. 52, no. 6, pp. 3486–3501, Jun. 2014.

[6] D. Pastina, F. Colone, T. Martelli, and P. Falcone, "Parasitic exploitation of Wi-Fi signals for indoor radar surveillance," *IEEE Trans. Veh. Technol.*, vol. 64, no. 4, pp. 1401–1415, Apr. 2015.

[7] D. Olivadese, E. Giusti, D. Petri, M. Martorella, A. Capria, and F. Berizzi, "Passive ISAR With DVB-T Signals," *IEEE Trans. Geosci. Remote Sens.*, vol. 51, no. 8, p. 4508–4517, Aug. 2013.

[8] W. Qiu *et al.*, "Compressive sensing-based algorithm for passive bistatic ISAR with DVB-T signals," *IEEE Trans. Aerosp. Electron. Syst.*, vol. 51, no. 3, pp. 2166–2180, Jul. 2015.

[9] M. K. Bączyk and K. Kulpa, "Moving target imaging in multistatic passive radar," *IET Radar, Sonar Navigat.*, vol. 13, no. 2, pp. 198–207, Feb. 2019.

[10] W. Feng, J.-M. Friedt, G. Cherniak, and M. Sato, "Passive radar imaging by filling gaps between ISDB digital TV channels," *IEEE J. Sel. Topics Appl. Earth Observ. Remote Sens.*, vol. 12, no. 7, pp. 2055–2068, Jul. 2019.

[11] J. L. Garry and G. E. Smith, "Passive ISAR part II: Narrowband imaging," *IET Radar, Sonar Navigat.*, vol. 13, no. 2, pp. 181–189, Feb. 2019.

[12] M. Golabi, A. Sheikhi, and M. Biguesh, "A new approach for sea target detection in satellite based passive radar," in *Proc. 21st Iranian Conf. Electr. Eng. (ICEE)*, Mashhad, Iran, May 2013, pp. 1–5.

[13] A. G. Stove, M. S. Gashinova, S. Hristov, and M. Cherniakov, "Passive maritime surveillance using satellite communication signals," *IEEE Trans. Aerosp. Electron. Syst.*, vol. 53, no. 6, pp. 2987–2997, Dec. 2017.

[14] Z. Li, F. Santi, D. Pastina, and P. Lombardo, "Passive radar array with low-power satellite illuminators based on fractional Fourier transform," *IEEE Sensors J.*, vol. 17, no. 24, pp. 8378–8394, Dec. 2017.

[15] H. Ma *et al.*, "Maritime moving target indication using passive GNSS-based bistatic radar," *IEEE Trans. Aerosp. Electron. Syst.*, vol. 54, no. 1, pp. 115–130, Feb. 2018.

[16] F. Santi, F. Pieralice, and D. Pastina, "Joint detection and localization of vessels at sea with a GNSS-based multistatic radar," *IEEE Trans. Geosci. Remote Sens.*, vol. 57, no. 8, pp. 5894–5913, Aug. 2019.

[17] D. Pastina, F. Santi, F. Pieralice, M. Antoniou, and M. Cherniakov, "Passive radar imaging of ship targets with GNSS signals of opportunity," *IEEE Trans. Geosci. Remote Sens.*, early access, Jul. 16, 2020, doi: 10.1109/TGRS.2020.3005306.

[18] S. Brisken, M. Moscadellli, V. Seidel, and C. Schwark, "Passive radar imaging using DVB-S2," in *Proc. IEEE RadarConf*, Seattle, WA, USA, May 2017, pp. 552–556.

[19] Z. Sun, T. Wang, T. Jiang, C. Chen, and W. Chen, "Analysis of the properties of DVB-S signal for passive radar application," in *Proc. Int. Conf. Wireless Commun. Signal Process.*, Hangzhou, China, Oct. 2013, pp. 1–5.

[20] D. Pastina, M. Sedehi, and D. Cristallini, "Passive bistatic ISAR based on geostationary satellites for coastal surveillance," in *Proc. IEEE Radar Conf.*, May 2010, pp. 865–870.

[21] J.-L. Barcena-Humanes, N. del-Rey-Maestre, M. P. Jarabo-Amores, D. Mata-Moya, and P. Gomez-del-Hoyo, "Passive radar imaging capabilities using space-borne commercial illuminators in surveillance applications," in *Proc. Signal Process. Symp. (SPSympo)*, Debe, Trinidad and Tobago, Jun. 2015, pp. 1–5.

[22] I. Pisciottano, D. Cristallini, J. Schell, and V. Seidel, "Passive ISAR for maritime target imaging: Experimental results," in *Proc. 19th Int. Radar Symp. (IRS)*, Bonn, Germany, Jun. 2018, pp. 1–10.

[23] T. V. Cao, R. Melino, and H.-T. Tran, "Using passive ISAR for imaging maritime targets," in *Proc. 20th Int. Radar Symp.*, Ulm, Germany, Jun. 2019, pp. 1–10.

[24] I. Pisciottano, D. Cristallini, and D. Pastina, "Maritime target imaging via simultaneous DVB-T and DVB-S passive ISAR," *IET Radar, Sonar Navigat.*, vol. 13, no. 9, pp. 1479–1487, Sep. 2019.

[25] F. Sadjadi, "Improved target classification using optimum polarimetric SAR signatures," *IEEE Trans. Aerosp. Electron. Syst.*, vol. 38, no. 1, pp. 38–49, Jan. 2002.

[26] M. Martorella, E. Giusti, A. Capria, F. Berizzi, and B. Bates, "Automatic target recognition by means of polarimetric ISAR images and neural networks," *IEEE Trans. Geosci. Remote Sens.*, vol. 47, no. 11, pp. 3786–3794, Nov. 2009.

[27] M. Martorella *et al.*, "Target recognition by means of polarimetric ISAR images," *IEEE Trans. Aerosp. Electron. Syst.*, vol. 47, no. 1, pp. 225–239, Jan. 2011.

[28] W. Qiu, H. Zhao, J. Zhou, and Q. Fu, "High-resolution fully polarimetric ISAR imaging based on compressive sensing," *IEEE Trans. Geosci. Remote Sens.*, vol. 52, no. 10, pp. 6119–6131, Oct. 2014.

[29] X. Bai, X. Zhou, F. Zhang, L. Wang, R. Xue, and F. Zhou, "Robust pol-ISAR target recognition based on ST-MC-DCNN," *IEEE Trans. Geosci. Remote Sens.*, vol. 57, no. 12, pp. 9912–9927, Dec. 2019.

[30] F. Colone and P. Lombardo, "Polarimetric passive coherent location," *IEEE Trans. Aerosp. Electron. Syst.*, vol. 51, no. 2, pp. 1079–1097, Apr. 2015.

[31] F. Filippini, F. Colone, D. Cristallini, and G. Bournaka, "Experimental results of polarimetric detection schemes for DVB-T-based passive radar," *IET Radar Sonar Nav.*, vol. 11, no. 6, pp. 883–891, Jun. 2017.

[32] A.-L. Germond, E. Pottier, and J. Saillard, "Foundations of bistatic radar polarimetry theory," *Proc. Radar*, vol. 97, no. 449, pp. 833–837, 1997.

[33] C. Titin-Schnaider, "Physical meaning of bistatic polarimetric parameters," *IEEE Trans. Geosci. Remote Sens.*, vol. 48, no. 5, pp. 2349–2356, May 2010.

[34] A. K. Mishra and B. Mulgrew, "Automatic target recognition using multipolar bistatic synthetic aperture radar," *IEEE Trans. Aero. Elect. Syst.*, vol. 46, no. 4, pp. 1906–1920, Oct. 2010.

[35] *Frequency Plan Satellites*. Accessed: Oct. 20, 2020. [Online]. Available: http://frequencyplansatellites.altervista.org/SES.html

[36] S. R. Cloude and E. Pottier, "A review of target decomposition theorems in radar polarimetry," *IEEE Trans. Geosci. Remote Sens.*, vol. 34, no. 2, pp. 498–518, Mar. 1996.

[37] S. R. Cloude and E. Pottier, "An entropy based classification scheme for land applications of polarimetric SAR," *IEEE Trans. Geosci. Remote Sens.*, vol. 35, no. 1, pp. 68–78, Jan. 1997.

[38] A. Danklmayer, "Application of principal component analysis in radar polarimetry," in *Proc. IEEE Geosci. Remote Sens. Symp. (IGARSS)*, vol. 3, Jul. 2005, p. 1999–2002.

[39] T. Dallmann and D. Heberling, "Principal component analysis for polarimetric radar cross-section imaging," in *Proc. 10th Eur. Conf. Antennas Propag. (EuCAP)*, Apr. 2016, pp. 1–5.

[40] L. M. Novak and M. C. Burl, "Optimal speckle reduction in polarimetric SAR imagery," *IEEE Trans. Aerosp. Electron. Syst.*, vol. 26, no. 2, pp. 293–305, Mar. 1990.

[41] L. M. Novak, M. B. Sechtin, and M. J. Cardullo, "Studies of target detection algorithms that use polarimetric radar data," *IEEE Trans. Aerosp. Electron. Syst.*, vol. 25, no. 2, pp. 150–165, Mar. 1989.

[42] I. Pisciottano, D. Cristallini, D. Pastina, and F. Santi, "Experimental results of polarimetric passive ISAR exploiting DVB-S2 illumination," in *Proc. IEEE RadarConf*, Washington, DC, USA, Apr. 2020, pp. 518–523.

[43] *ASTRA 1KR's Mission*. Accessed: Oct. 20, 2020. [Online]. Available: https://www.ses.com/our-coverage#/explore/search?type=satellite&q=335

[44] W. Melvin and J. Scheer, *Principles of Modern Radar: Advanced Techniques*. London, U.K.: Institution of Engineering and Technology, 2012.

[45] A. Manno-Kovacs, E. Giusti, F. Berizzi, and L. Kovacs, "Image based robust target classification for passive ISAR," *IEEE Sensors J.*, vol. 19, no. 1, p. 268–276, Jan. 2019.

Iole Pisciottano (Graduate Student Member, IEEE) received the master's degree in telecommunication engineering from "Federico II" University of Naples, Italy, in March 2011.

From June 2010 to December 2010, she carried on research activity with the Polarimetric SAR Interferometry (Pol-InSAR) Group, DLR Microwaves and Radar Institute, Germany. From June 2011 to November 2014, she was a Research Scientist with the Ultra Wide Band Team in the Passive Radar Anti Jamming Techniques and Classification Department, Fraunhofer Institute for High Frequency Physics and Radar Techniques FHR, Wachtberg, Germany. Since April 2017, she has been with the Passive Covert Radar Team in the Passive Radar and Anti Jamming Techniques Department, Fraunhofer Institute FHR. She is currently a Doctoral Researcher with the Department of Information Engineering, Electronics and Telecommunications, Sapienza University of Rome. Her research interests include ISAR image processing and polarimetric data analysis for passive radar systems. She is involved in scientific research projects funded by the European Defence Agency.

Fabrizio Santi (Member, IEEE) received the master's *(cum laude)* degree in telecommunication engineering and the Ph.D. degree in remote sensing from the Sapienza University of Rome, Italy, in September 2010 and June 2014, respectively.

From April 2013 to September 2013, he carried on research activity with the Microwave Integrated Systems Laboratory, University of Birmingham, U.K. He is currently a Postdoctoral Researcher with the Department of Information Engineering, Electronics and Telecommunications, Sapienza University of Rome. He is involved in scientific research projects funded by the European Commission, the Italian Space Agency, and the national radar industry. The results of his research activity have been reported in a number of journals and conference papers. His main research interests include SAR/ISAR radar imaging and space-based active and passive radar systems.

Dr. Santi received the Best Italian Thesis on Remote Sensing Award from the IEEE Geoscience and Remote Sensing South Italy Chapter in 2010. He is a member of the Editorial Board of the *International Journal of Electronics and Communications* (AEÜ, Elsevier) and Topic Editor of the journal *Remote Sensing* (MDPI).

Debora Pastina (Member, IEEE) received the Laurea degree in telecommunications engineering and the Ph.D. degree in information and communication engineering from the Sapienza University of Rome, Rome, Italy, in 1996 and 2000, respectively.

From July 1998 to March 1999, she carried on research activity with the SAR Processing Team, Defence Evaluation Research Agency (DERA), Malvern, U.K. In March 2001, she joined as an Assistant Professor with the University of Rome "La Sapienza," DIET Department, where she is currently an Associate Professor, teaching several courses related to remote sensing and telecommunications. She is involved in and is responsible of scientific research projects funded by the Italian Ministry of Research, the Italian Space Agency, the European Commission, and the National Radar Industry. The results of her research activity have been reported in a number of journal and conference papers. Her main research interests include SAR/ISAR signal processing, ground moving target indication techniques, GNSS-based passive radar systems, FSR systems, clutter models, coherent and incoherent radar detection in non-Gaussian clutter, and CFAR radar techniques.

Dr. Pastina was the Chairman of the Local Committee of the IEEE/ISPRS Joint Workshop on Remote Sensing and Data Fusion over Urban Areas (Rome, November 2001). She was the Publication Chair of the 2008 IEEE Radar Conference held in Rome in May 2008. She is a member of the Editorial Board of the *International Journal of Electronics and Communications* (AEÜ, Elsevier) acting as an Area Editor for *Radar Systems and Techniques*. She serves as an Associate Editor for Radar Systems for the IEEE TRANSACTIONS ON AEROSPACE AND ELECTRONIC SYSTEMS. She has served in the technical review committee for many international conferences on radar systems and remote sensing. She is also a frequent reviewer for a number of international technical journals.

Diego Cristallini was born in Terni, Italy, in 1981. He graduated *(cum laude)* in telecommunication engineering from the University of Rome "La Sapienza" in May 2006, and received the Ph.D. degree in radar remote sensing from the University of Rome "La Sapienza" in April 2010, with a thesis entitled "Innovative adaptive techniques for multi-channel spaceborne SAR systems."

From December 2009 to February 2015, he was with the Array-based Radar Imaging Department, Fraunhofer Institute for High-Frequency Physics and Radar Techniques FHR, Wachtberg, Germany. During this time, he has been working on the development of innovative space-time adaptive techniques for clutter suppression in multi-channel airborne radar systems, with special attention to bistatic systems and to highly non-homogeneous clutter environments. Since March 2015, he has been leading the team on Passive Covert Radar in the Passive Radar and Anti-Jamming Techniques Department, Fraunhofer FHR, Germany.

Dr. Cristallini received the Best Paper Award at EUSAR 2014, has coauthored the Best Poster Award at EUSAR 2018, and was a co-recipient of the 2018 Premium Award for Best Paper in IET Radar, Sonar and Navigation. He is the Co-Chair of the NATO-SET 242 Group on "PCL on moving platforms" and has been lecturing for the NATO LS-243 "Passive Radar Technology."